

DSCC2016-9923

EXPERIMENTAL GAIT ANALYSIS OF WAVEBOARD LOCOMOTION

Ayush Agrawal

Hesham M. Zaini

Department of Mechanical Engineering
Carnegie Mellon University
Pittsburgh, Pennsylvania 15213
ayusha@andrew.cmu.edu
hmzaini@andrew.cmu.edu

Tony Dear

Howie Choset

The Robotics Institute
Carnegie Mellon University
Pittsburgh, Pennsylvania 15213
tonydear@cmu.edu
choset@cs.cmu.edu

ABSTRACT

Through modeling and experimentation, we analyze common gaits on a waveboard, an underactuated mechanical system whose motion is governed by both nonholonomic constraints and momentum conservation. We take advantage of the system's symmetries to derive a reduced system model that differentiates between kinematic and dynamic components of motion. We evaluate this model using marker trajectory data gathered through an optical tracking system for various types of gaits. By extracting relevant trajectory parameters via state reconstruction and fitting our joint variables to an ellipse, we determine the kinematic components of gaits commonly used by human riders. In particular, we demonstrate that traditional forward motion is purely dynamic, while sustained turning motion contains kinematic components. In order to validate our model, we compare experimentally obtained trajectories with reconstructed displacements based on the model. Finally, we suggest an approach for further analysis of the dynamic components of these gaits.

INTRODUCTION

The waveboard, also known as the essboard, caster board, vigor board, and ripstik, is a skateboard variant in which two platforms, each resting upon a caster wheel, are constrained to rotate about the same axis and coupled with a torsional spring. It is a mixed mechanical system whose motion is governed by both nonholonomic velocity constraints and momentum conservation. It is modeled similarly to the variable inertia snakeboard examined by Shamma et al. [1], who used geometric mechanics to differentiate between kinematic and dynamic components of motion.

Relative to traditional two-wheel drive systems, the waveboard possesses greater maneuverability and potentially higher efficiency at the expense of stability. Modeling insight could be used by designers to optimize kinematic parameters of

waveboards in light of ergonomic considerations. More generally, analysis of the locomotive capabilities of this system informs control and planning of highly dynamic mobile robots.

Although the waveboard itself has not appeared often in geometric mechanics literature, the snakeboard is a similar system that has received considerable attention in the context of underactuated systems and controllability of nonholonomic mechanical systems. The snakeboard was first analyzed as a nonholonomic mechanical system by Ostrowski et al. [2]. Shamma et al. [1] analyzed and generated gaits for mixed mechanical systems using height functions to analyze geometric phase shift, as well as a novel scaled momentum and gamma functions to evaluate dynamic phase shift. In [1, 3], Shamma et al. classified gaits into three different categories: purely kinematic, purely dynamic, and kino-dynamic. More recently, Shamma and de Oliveira provided an analytical solution to snakeboard motion planning [4]. Dear et al. [5] built upon their work using body coordinates and local trajectory information to address trajectory generation. Dear et al. [6] also incorporated dissipative friction in the traveling direction and skidding in the snakeboard model, investigating these effects on trajectory planning. Asnafi and Mahzoon [7] generated some flower-like gaits for the snakeboard. Similar geometric approaches can be applied to the waveboard in order to analyze its locomotive capabilities.

This paper addresses the challenge of modeling and characterizing motions of the waveboard. In the next section, we present a model for the waveboard and derive its reconstruction equation. Subsequent sections describe experimental methodology and analysis of common types of gaits in the framework of geometric mechanics. Correlations between configurational variations and trajectory parameters are investigated, and numerically reconstructed forward motion displacements are compared with experimental data.

WAVEBOARD MODELING

The waveboard consists of two platforms coupled with a torsional spring and constrained to rotate along the same axis. Each platform rests upon a caster wheel that is inclined relative to the vertical axis. A schematic of the waveboard, illustrating relevant model parameters, is presented in Fig. 1. Here, m_1 represents the mass of the entire system, m_2 half the mass of the rider, L_1 the separation between the center of the waveboard and each wheel, L_2 the height of idealized mass m_2 above each platform, and J the moment of inertia of the system about the vertical axis coincident with the board center (not shown).

To obtain a dynamical model of the waveboard, we first derive the equations of motion by solving the Euler-Lagrange equations in generalized coordinates, as demonstrated by Kinugasa et al. [8]. We take advantage of the *trivial fiber bundle* structure of the configuration space and decompose it into a *base space*, which describes internal shape changes of the system, and a *fiber space*, which describes position and orientation with respect to an inertial frame. Inherent symmetries render the Lagrangian and nonholonomic constraints invariant to global position and orientation, allowing us to obtain a simplified and reduced form of the equations of motion in body coordinates. The fiber bundle structure allows us to study the effects of internal shape changes on motion in the inertial frame through a first order differential equation known as the *reconstruction equation*. This enables us to intuitively visualize kinematic contributions of various periodic internal shape changes (gaits) for further analysis.

Model Assumptions

The following assumptions are made in order to simplify model derivation, and are similar to those in [8].

- Roll angles of the front and back platforms are small, permitting the following small angle approximations.

$$\sin(\phi_i) \approx \phi_i \quad (1)$$

$$\cos(\phi_i) \approx 1 \quad (2)$$

where $i = f, b$ for the front and back platforms.

- The front and back roll angles alone span the entire shape space of the board. Wheel dynamics are ignored, and the following holonomic constraints map platform roll angles surjectively onto wheel yaw angles by the relation

$$\tan(\psi_i) = \tan(\alpha) \sin(\phi_i), \quad (3)$$

where $i = f, b$, and α is the constant angle of wheel inclination.

- Dissipative elements within the system are neglected.

Lagrangian Mechanics

The configuration of the waveboard, Q , is a trivial principal fiber bundle. $Q = G \times M$, where G , the fiber space with a Lie group structure, represents the position of the waveboard with respect to an inertial coordinate frame, comprising of position

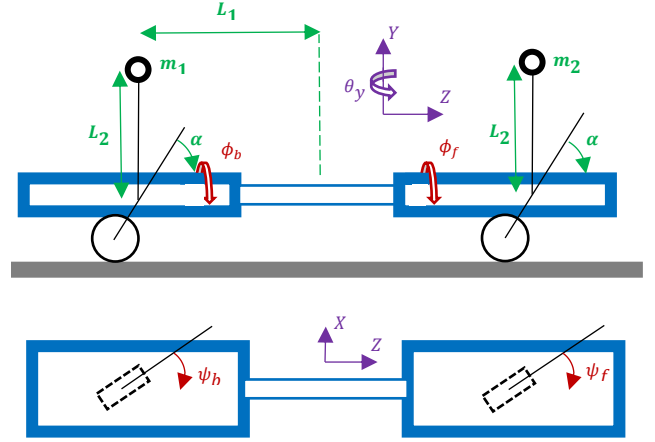


FIGURE 1. DIAGRAMS OF WAVEBOARD MODEL, ILLUSTRATING SIDE VIEW (TOP) AND TOP VIEW (BOTTOM). ANNOTATED MODEL PARAMETERS INCLUDE CONSTANTS (GREEN), JOINT VARIABLES (RED), AND AN INERTIAL FRAME (VIOLET)

and orientation variables z , x , and θ of the waveboard. M , the base space, represents the internal degrees of freedom of the waveboard, comprising of roll angles ϕ_f and ϕ_b of the front and back platforms respectively, measured about the z -axis of the body frame relative to the x - z plane. A configuration variable can then be expressed as $q = (g, r) \in Q$ where $g \in G$ and $r \in M$. Similarly, a configuration velocity can then be written as $\dot{q} = (\dot{g}, \dot{r})$, where \dot{q} represents the configuration velocity. Since the roll angles ϕ_f and ϕ_b are small, the potential energy of the system remains fairly constant. This allows us to define the Lagrangian as the total kinetic energy of the system in the form

$$L = \frac{1}{2} \dot{q}^T M \dot{q}, \quad (4)$$

where M is the mass matrix. The Lagrangian of the waveboard [8] can be expressed explicitly as

$$L = \frac{1}{2} m_1 (\dot{z}^2 + \dot{x}^2) + \frac{1}{2} J \dot{\theta}^2 + \frac{1}{2} m_2 \left[\left(\frac{d}{dt} [z + L_1 \cos(\theta) - L_2 \phi_f \sin(\theta)] \right)^2 + \left(\frac{d}{dt} [x + L_1 \sin(\theta) + L_2 \phi_f \cos(\theta)] \right)^2 + \left(\frac{d}{dt} [z - L_1 \cos(\theta) - L_2 \phi_b \sin(\theta)] \right)^2 + \left(\frac{d}{dt} [x - L_1 \sin(\theta) + L_2 \phi_b \cos(\theta)] \right)^2 \right]. \quad (5)$$

Nonholonomic Constraints

Two nonholonomic constraints act upon the waveboard, namely, a no-slide condition on each of the two caster wheels [8]. These constraints are expressed in Pfaffian form as follows.

$$\omega(q) \dot{q} = \begin{bmatrix} \sin(\theta + \psi_f) & -\cos(\theta + \psi_f) & -L_1 \cos(\psi_f) & 0 & 0 \\ \sin(\theta + \psi_b) & -\cos(\theta + \psi_b) & L_1 \cos(\psi_b) & 0 & 0 \end{bmatrix} \begin{bmatrix} \dot{x} \\ \dot{y} \\ \dot{\theta} \\ \dot{\phi}_f \\ \dot{\phi}_b \end{bmatrix} = 0 \quad (6)$$

The waveboard possesses fewer nonholonomic constraints than fiber variables, and is therefore a mixed mechanical system

[1, 3]. In other words, since the number of constraints is not sufficient to specify the full motion of the entire position space, the system is also governed by Lagrangian mechanics. The dynamic equations of motion of this type of system can be expressed in the form

$$\frac{d}{dt} \left(\frac{\partial L}{\partial \dot{q}_i} \right) - \frac{\partial L}{\partial q_i} + \lambda_j \omega_i^j = \tau_i, \quad (7)$$

where $i = 1, 2, \dots, 5$ for each dimension of the configuration space, $j = 1, 2$ for each nonholonomic constraint, ω_i^j is the $(j, i)^{\text{th}}$ component of ω , $\lambda = [\lambda_1 \ \lambda_2]^T$ is the set of Lagrange multipliers, and $\tau = [\tau_1 \ \tau_2]^T$ is the set of generalized forces.

Body Representation

For configuration spaces with a Lie group structure, we can define an action Φ_g on the configuration manifold and a lifted action $T_g \Phi_g$ on its tangent space $T_q Q$. The body velocity ξ , which is an element of the Lie Algebra, is expressed as

$$\xi = \begin{bmatrix} \xi^z \\ \xi^x \\ \xi^\theta \end{bmatrix} = T_g L_g^{-1} \dot{g}, \quad (8)$$

where L_g represents the left action on the fiber variables and $T_g L_g$ represents the left lifted action. In terms of the system model, this is simply the velocity of the system represented in a body-fixed frame attached to the center of the waveboard.

The system dynamics are symmetric with respect to the fiber variables, a fact we can easily exploit using our principal bundle structure to derive a reduced set of dynamics. This property applies to both the Lagrangian and the nonholonomic constraints, i.e.

$$L(q, \dot{q}) = L(\Phi_g q, T_g \Phi_g \dot{q}) \quad (9)$$

$$\omega(q) \dot{q} = \omega(\Phi_g q) T_g \Phi_g \dot{q} \quad (10)$$

Utilizing this property, the dependence of the Lagrangian and nonholonomic constraints on the fiber variables is eliminated by expressing the dynamics of the system at the Lie group identity [9]. The reduced Lagrangian l , computed by substituting Eq. (8) into Eq. (9), has the form

$$l(\xi, \dot{r}) = \frac{1}{2} [\xi^T \ \dot{r}^T] \tilde{M} \begin{bmatrix} \xi \\ \dot{r} \end{bmatrix}, \quad (11)$$

where \tilde{M} is the reduced mass matrix

$$\tilde{M} = \begin{bmatrix} I(r) & I(r) A(r) \\ A^T(r) I^T(r) & m(r) \end{bmatrix}, \quad (12)$$

in which A is the local form of the mechanical connection and I is the local form of the locked inertia tensor [1, 3], which is expressed as follows for the waveboard.

$$I = \begin{bmatrix} m_1 + 2m_2 & 0 & -L_2 m_2 (\phi_f + \phi_b) \\ 0 & m_1 + 2m_2 & 0 \\ -L_2 m_2 (\phi_f + \phi_b) & 0 & J + m_2 (2L_1^2 + L_2^2 (\phi_f^2 + \phi_b^2)) \end{bmatrix} \quad (13)$$

Note that the mass matrix varies with configuration, whose space is spanned by base variables ϕ_f and ϕ_b . Thus, the waveboard is similar to the variable inertia snakeboard defined in [1, 3], whose mass matrix is also expressed as a function of base variables.

Similarly, by substituting Eq. (8) into Eq. (6), we can compute the nonholonomic constraints in body coordinates as

$$\omega(r) \begin{bmatrix} \xi \\ \dot{r} \end{bmatrix} = \omega_\xi(r) \xi + \omega_r(r) \dot{r} = 0. \quad (14)$$

For the waveboard, ω_ξ is

$$\omega_\xi = \begin{bmatrix} \frac{\sin(\phi_f) \tan(\alpha)}{\sqrt{\sin^2(\phi_f) \tan^2(\alpha) + 1}} & -\frac{1}{\sqrt{\sin^2(\phi_f) \tan^2(\alpha) + 1}} & -\frac{L_1}{\sqrt{\sin^2(\phi_f) \tan^2(\alpha) + 1}} \\ \frac{\sin(\phi_b) \tan(\alpha)}{\sqrt{\sin^2(\phi_b) \tan^2(\alpha) + 1}} & -\frac{1}{\sqrt{\sin^2(\phi_b) \tan^2(\alpha) + 1}} & -\frac{L_1}{\sqrt{\sin^2(\phi_b) \tan^2(\alpha) + 1}} \end{bmatrix} \quad (15)$$

and $\omega_r = \mathbf{0}^{2 \times 2}$.

The reduced equations of motion then become

$$\frac{d}{dt} \left(\frac{\partial l}{\partial \xi} \right) + ad_\xi^* \frac{\partial l}{\partial \xi} + \lambda^T \bar{\omega} = 0 \quad (16)$$

$$\frac{d}{dt} \left(\frac{\partial l}{\partial \dot{r}} \right) - \frac{\partial l}{\partial r} = \tau_j^r, \quad (17)$$

where $j = 1, 2$, τ_j^r is the set of base forcing functions [10], and ad_ξ^* is the dual adjoint operator on the Lie algebra.

Kinematic and Dynamic Reconstruction

The waveboard is a mixed mechanical system in which the nonholonomic constraints alone are not sufficient to completely specify the system's fiber velocity for a given base velocity. We can derive a first-order reconstruction equation [1, 3] of the form

$$\xi = -\mathbf{A}(r) \dot{r} + \Gamma(r) p^T, \quad (18)$$

where $\mathbf{A}(r)$ is the local form of the mixed mechanical connection and $\Gamma(r)$ is an implicit function of r . This equation naturally follows the principal bundle structure of the system wherein trajectories in the base are lifted to trajectories in the fiber via $\mathbf{A}(r)$.

Note that Eq. (18) presents the body velocity as a sum of two separate components. The first term is the kinematic contribution, which arises purely from joint movement. The second term is a dynamic or drift component, where p is the generalized nonholonomic momentum defined as

$$p = \frac{\partial l}{\partial \xi} \bar{\Omega}^T = (\xi^T I^T + \dot{r} (IA)^T) \bar{\Omega}^T, \quad (19)$$

TABLE 1. ELEMENTS OF $\mathbf{A}(r)$ MATRIX

$D_A = \tan^2(\alpha) \left((\sin^2(\phi_f) + \sin^2(\phi_b)) (0.25J + L_1^2(0.25m_1 + m_2) + L_2^2m_2(0.25\phi_f^2 + 0.25\phi_b^2)) - 0.5 \sin(\phi_f) \sin(\phi_b) (J - L_1^2m_1 + L_2^2m_2(\phi_f^2 + \phi_b^2)) \right) + L_1L_2m_2 \tan(\alpha) (\phi_f + \phi_b) (\sin(\phi_b) - \sin(\phi_f)) + L_1^2(m_1 + 2m_2)$	
$A_{11} = L_1^2L_2m_2 \tan(\alpha) \sin(\phi_f)$	$A_{12} = L_1^2L_2m_2 \tan(\alpha) \sin(\phi_b)$
$A_{21} = 0.5L_1^2L_2m_2 \tan^2(\alpha) \sin(\phi_f) (\sin(\phi_f) + \sin(\phi_b))$	$A_{22} = 0.5L_1^2L_2m_2 \tan^2(\alpha) \sin(\phi_b) (\sin(\phi_f) + \sin(\phi_b))$
$A_{31} = 0.5L_1^2L_2m_2 \tan^2(\alpha) \sin(\phi_f) (\sin(\phi_f) - \sin(\phi_b))$	$A_{32} = 0.5L_1^2L_2m_2 \tan^2(\alpha) \sin(\phi_f) (\sin(\phi_f) - \sin(\phi_b))$

TABLE 2. ELEMENTS OF $\Gamma(r)$ MATRIX

$D_r = \tan^2(\alpha) \left((\sin^2(\phi_f) + \sin^2(\phi_b)) (J + L_1^2(m_1 + 4m_2) + L_2^2m_2(\phi_f^2 + \phi_b^2)) - 2 \sin(\phi_f) \sin(\phi_b) (J - L_1^2m_1 + L_2^2m_2(\phi_f^2 + \phi_b^2)) \right) + 4L_1L_2m_2 \tan(\alpha) (\phi_f + \phi_b) (\sin(\phi_b) - \sin(\phi_f)) + 4L_1^2(m_1 + 2m_2)$		
$\Gamma_1 = 2L_1 \tan(\alpha) (\sin(\phi_f) - \sin(\phi_b))$	$\Gamma_2 = L_1 \tan^2(\alpha) (\sin^2(\phi_f) - \sin^2(\phi_b))$	$\Gamma_3 = \tan^2(\alpha) (\sin(\phi_f) - \sin(\phi_b))^2$

where $\bar{\Omega}^T$ is the null space of ω_ξ . In general, the system's momentum components evolve in a way that satisfies the nonholonomic constraints.

From Eq. (14) and (19), we can derive the reconstruction equation to be

$$\xi = \begin{bmatrix} \omega_\xi \\ \bar{\Omega} I \end{bmatrix}^{-1} \begin{bmatrix} \mathbf{0}^{k \times k} \\ (p^T)^{l-k} \end{bmatrix} - \begin{bmatrix} \omega_\xi \\ \bar{\Omega} I \end{bmatrix}^{-1} \begin{bmatrix} \omega_r \\ \bar{\Omega} I A \end{bmatrix} \dot{r}. \quad (20)$$

The reader is referred to [1, 3] for a proof. For the waveboard, $\mathbf{A}(r)$ and $\Gamma(r)$ are expressed in the following forms.

$$\mathbf{A}(r) = \frac{1}{D_A} \begin{bmatrix} A_{11} & A_{12} \\ A_{21} & A_{22} \\ A_{31} & A_{32} \end{bmatrix} \quad (21)$$

$$\Gamma(r) = \frac{1}{D_\Gamma} \begin{bmatrix} \Gamma_1 \\ \Gamma_2 \\ \Gamma_3 \end{bmatrix} \quad (22)$$

Symbolic expressions of the subcomponents are presented in Table 1 and Table 2.

The generalized nonholonomic momentum variables are governed by a first order differential equation. Specifically, for systems such as the waveboard in which the number of nonholonomic constraints are one less than the number of fiber

variables, this first order differential equation is expressed in the following form.

$$\dot{p} = \dot{r}^T \sigma_{\dot{r}\dot{r}} \dot{r} + \dot{r}^T \sigma_{\dot{r}p} p, \quad (23)$$

where $\sigma_{\dot{r}\dot{r}}$ and $\sigma_{\dot{r}p}$ are matrices that depend only on r [11].

Height Functions

Having obtained $\mathbf{A}(r)$ and $\Gamma(r)$, we can integrate each row of Eq. (18) with respect to time to compute the body velocity integral of the waveboard [12]. From [1, 3], we know that this integral is equal to the sum of two integrals: the geometric phase shift I^{GEO} and the dynamic phase shift I^{DYN} . In particular, the geometric phase shift is expressed as

$$I^{GEO} = \int_{t_0}^{t_1} -\mathbf{A}(r) \dot{r} dt = \oint_{r(t_0)}^{r(t_1)} -\mathbf{A}(r) dr. \quad (24)$$

Each row of the integrand in the rightmost expression is a one-form, hence the line integral can be converted to a volume integral as follows.

$$I^{GEO} = \iint_{\Phi} \text{curl } \mathbf{A}(r) dr, \quad (25)$$

where Φ is the region enclosed by the gait ϕ in the base space. The integrand of the above equation is known as the height

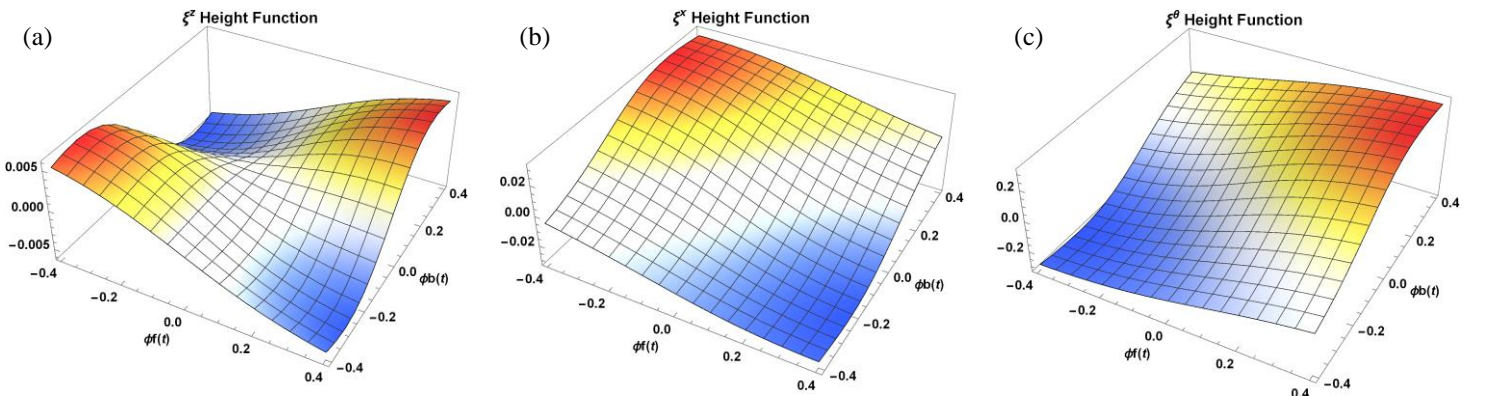


FIGURE 2. HEIGHT MAPS OF WAVEBOARD FOR (A) FORWARD MOTION, (B) LATERAL MOTION, AND (C) ROTATION ABOUT THE VERTICAL AXIS.

function [1, 3]. For a two-dimensional base space, the height function for each fiber direction is

$$F_i(r^1, r^2) = \frac{\partial A_2^i}{\partial r_1} - \frac{\partial A_1^i}{\partial r_2}, \quad (26)$$

where $i = 1, 2, 3$ for each fiber variable. We use the estimated parameters in Table 3, which correspond with our physical system, to calculate values of the height functions for ξ^z , ξ^x , and ξ^θ , which are plotted in Fig. 2.

The height functions allow us to visualize the geometric phase shift corresponding to various gaits. Since this base space is two-dimensional, we can visualize geometric phase shift as volume beneath the graph of the height functions within a gait. In turn, gaits that enclose zero area in the base space, as in Fig. 5(a, b, c, and e), are not associated with any volume, hence geometric phase shift is zero for these gaits.

We note that the ξ^z height function plotted in Fig. 2(a) is antisymmetric about $\phi_f = 0$ and $\phi_b = 0$. Therefore, any gait that is symmetric about either axis encloses equal areas in regions with opposite sign, having no net volume, and thus zero geometric phase shift in the z -direction. Similarly, the ξ^x and ξ^θ height functions, plotted in Fig. 2(b) and 2(c), are antisymmetric about $\phi_f = \phi_b$ and $\phi_f = -\phi_b$, respectively. Thus, any gait symmetric about these axes encloses equal areas in regions with opposite sign, having zero geometric phase shift in these fiber directions.

TABLE 3. MODEL PARAMETERS

Symbol	Description	Value
m_1	Mass of the entire system	71 kg
m_2	Half mass of rider	35 kg
L_1	Separation between board center and each wheel	0.095 m
L_2	Height of mass m_2 above each platform	0.100 m
J	Mass moment of inertia of system about vertical axis	0.64 kg m ²
α	Angle of inclination of caster wheel axis relative to horizontal axis	70°

EXPERIMENTAL METHODOLOGY

Gait analysis of physical motions of a waveboard require state identification throughout the duration of the gait. This was accomplished through reconstruction of marker trajectory data obtained using optical tracking techniques.

Optical Tracking of Waveboard State

Computer vision techniques were used to track the state of the system at frequent time intervals throughout the course of each gait. Four cameras mounted to the ceiling at various positions and orientations captured the motion of markers fixed to various parts of the board. Optical tracking software was used to reconstruct the three-dimensional position of each marker at 120 frames per second. A photograph of the overall setup is presented in Fig. 3.

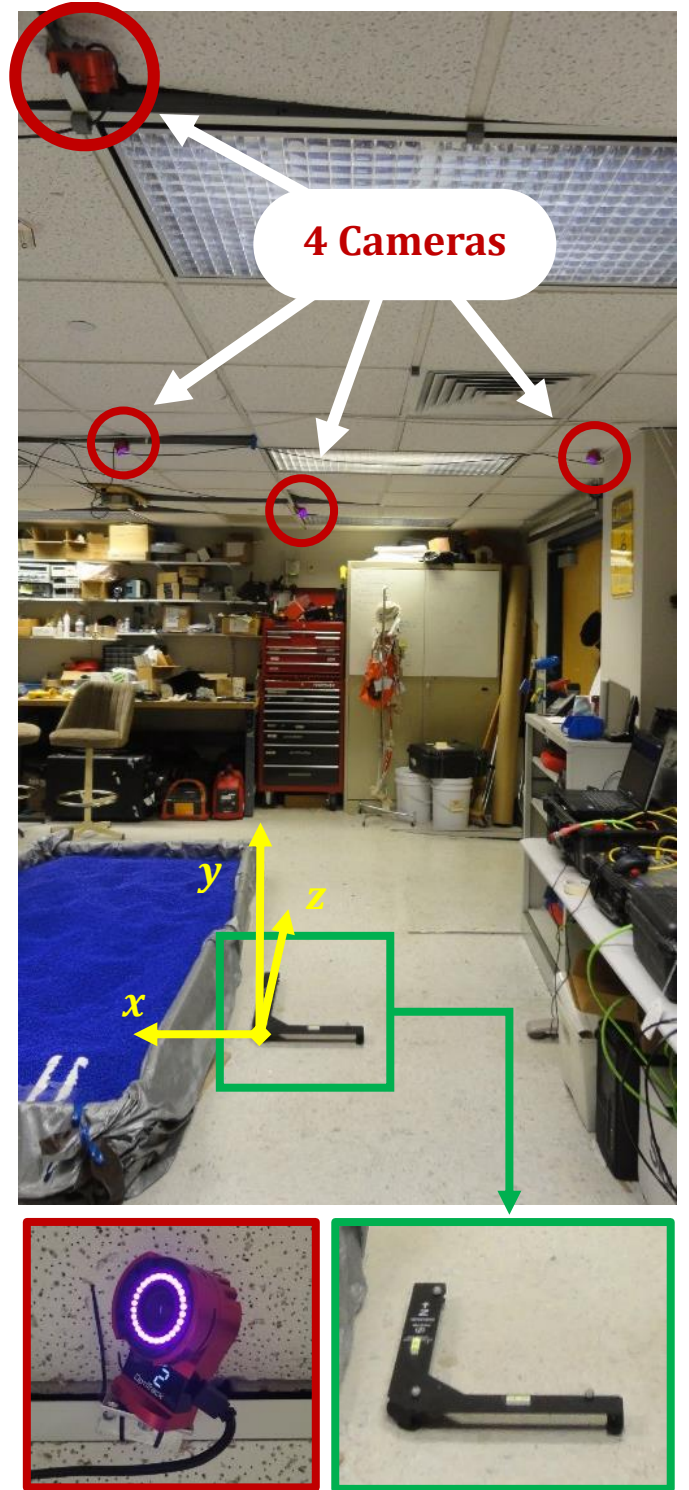


FIGURE 3. PHOTOGRAPHS OF EXPERIMENTAL APPARATUS FOR OPTICAL TRACKING OF WAVEBOARD STATE. TOP: OVERALL SETUP, ILLUSTRATING GLOBAL COORDINATE SYSTEM (YELLOW) AND CAMERA MOUNTING LOCATIONS (RED). LOWER LEFT: ONE OF FOUR CAMERAS USED FOR OPTICAL TRACKING. LOWER RIGHT: CALIBRATION DEVICE USED TO DEFINE ORIGIN AND ORIENTATION OF GLOBAL COORDINATE FRAME.

Four reflective markers were adhered to the waveboard with adhesive foam. Two markers on each platform were used to reconstruct the position and handedness of both platforms. Marker orientation is presented in Fig. 4. The position, orientation, and configuration of the waveboard throughout each gait were obtained from processed optical tracking data.

Gait Generation

Various gaits were performed on the waveboard by a rider within the field of vision of the cameras. Some types of gaits for sustained forward motion are illustrated in Fig. 5. Note that linear base space motions enclose zero area, having no kinematic contributions, and are thus associated with purely dynamic gaits. Amplitude of oscillation was varied for forward motions where neither leg was idle, while frequency of oscillation was varied for forward motions with an idle leg. A total of 76 gaits were performed on the waveboard.

Data Processing

Post processing of optical tracking data comprised of marker identification, state reconstruction, curve fitting, and data visualization. First, markers were manually identified based on their relative positions within the global coordinate frame. Waveboard configuration was determined based on the relative positions of the markers. Measurements of marker placement were coupled with these data to calculate the relative position of the center of the board. Global orientation of the board was calculated by vector dot products between axes of global and body coordinate frames. Finally, absolute positions of the markers in the global frame were used to determine the position of the center of the board in global coordinates. Thus, full state reconstruction of the waveboard was achieved from marker tracking data.

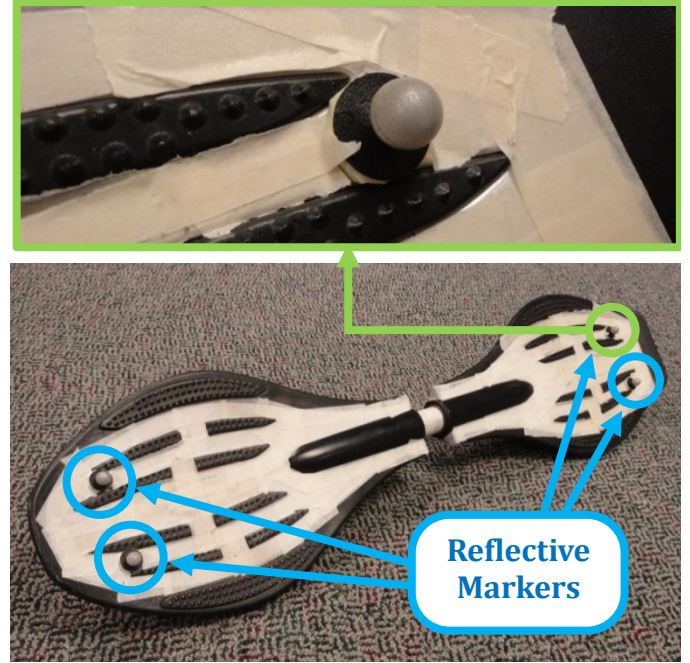


FIGURE 4. PHOTOGRAPHS ILLUSTRATING MARKER PLACEMENT ON THE WAVEBOARD. MARKERS WERE FIXED TO THE BOARD USING ADHESIVE FOAM PADS (TOP).

Curve fitting of the time variation of base variables was used to precisely quantify gait parameters and reduce noise. All gaits resulting in sustained forward motion were assumed to have sinusoidal inputs of the form

$$\phi_i = A_i \sin(\omega_i t - \Delta_i) + B_i, \quad (27)$$

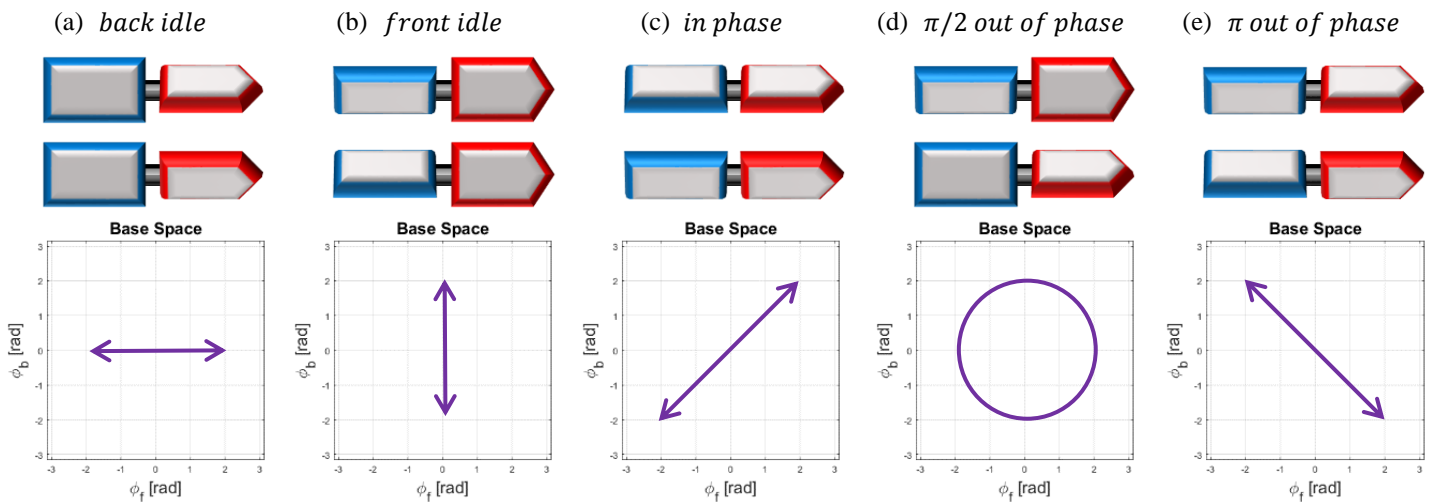


FIGURE 5. DIAGRAMS ILLUSTRATING GAITS PERFORMED ON THE WAVEBOARD. FOR EACH GAIT, BOARD CONFIGURATIONS (TOP) AND BASE SPACE MOTIONS (BOTTOM) ARE ILLUSTRATED. NOTE THAT STRAIGHT LINES ARE HIGH ASPECT RATIO ELLIPSES, AND THAT BASE SPACE MOTIONS ARE COUNTERCLOCKWISE SINCE REAR LEG MOTION TRAILS FRONT LEG MOTION.

where $i = f, b$ for the front and back platforms, and t is time. Nonlinear least-squares optimization techniques were used to solve for values of constants A_i , ω_i , Δ_i , and B_i , which are oscillation amplitude, oscillation frequency, phase offset, and roll angle offset bias, respectively. The phase lag Δ_0 of back platform oscillation relative to front platform oscillation is computed as

$$\Delta_0 = \Delta_b - \Delta_f. \quad (28)$$

By the definition of a gait as a periodic motion, the oscillation frequencies of the front and back platforms should be identical and are thus averaged in presentation of fitted parameters.

RESULTS

Plots of relevant parameters for each type of gait that was performed are qualitatively analyzed. Experimentally obtained base space motions are superimposed on the height maps presented in Fig. 2 to determine the geometric phase shift for various types of gaits. Equation (19) was used to compute the generalized nonholonomic momentum for the duration of motion, and Eq. (8) and (18) were used to compute the fiber velocity \dot{g} in the global frame. The global velocity was then integrated to compute displacement in the global frame, resulting in an approximate measure of the translational component of the displacement.

A traditional gait for forward motion on the waveboard is presented in Fig. 6. Forward velocity remains fairly constant. We immediately observe from the shape of the ellipse in Fig. 6(a) that the motion is more out of phase than in phase, due to the downward slope of the major axis of the ellipse. A phase lag of

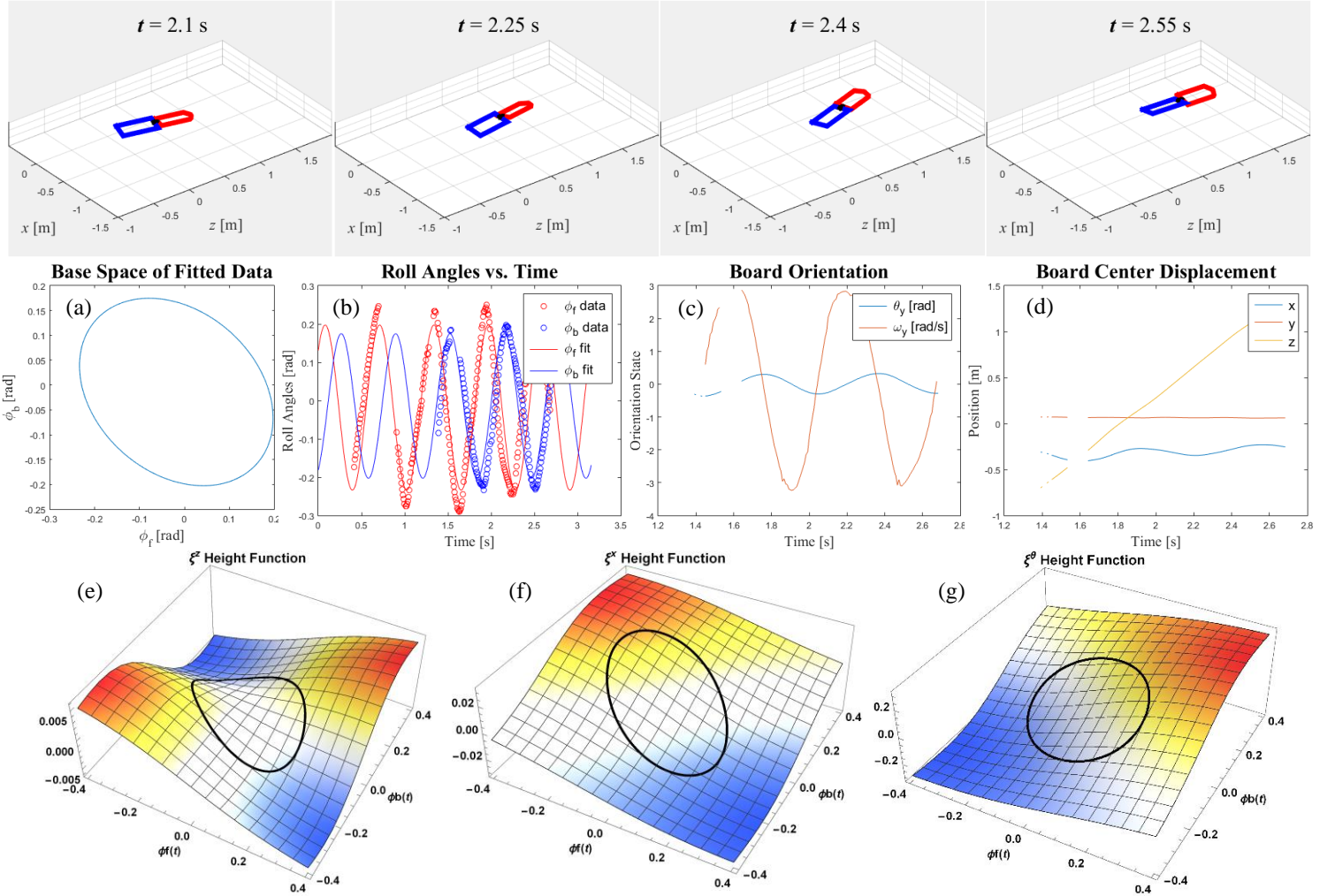


FIGURE 6. TRADITIONAL GAIT FOR SUSTAINED FORWARD MOTION OF THE WAVEBOARD. TOP ROW: ANIMATION SEQUENCES. MIDDLE ROW: PLOTS ILLUSTRATING (A) BASE SPACE OF FITTED DATA, AND TIME VARIATIONS OF (B) ROLL ANGLES, (C) BOARD ORIENTATION STATES, AND (D) BOARD CENTER DISPLACEMENT. BOTTOM ROW: BASE SPACE OVERLAID ON HEIGHT FUNCTIONS FOR (E) FORWARD MOTION, (F) LATERAL MOTION, AND (G) ROTATION ABOUT THE VERTICAL AXIS.

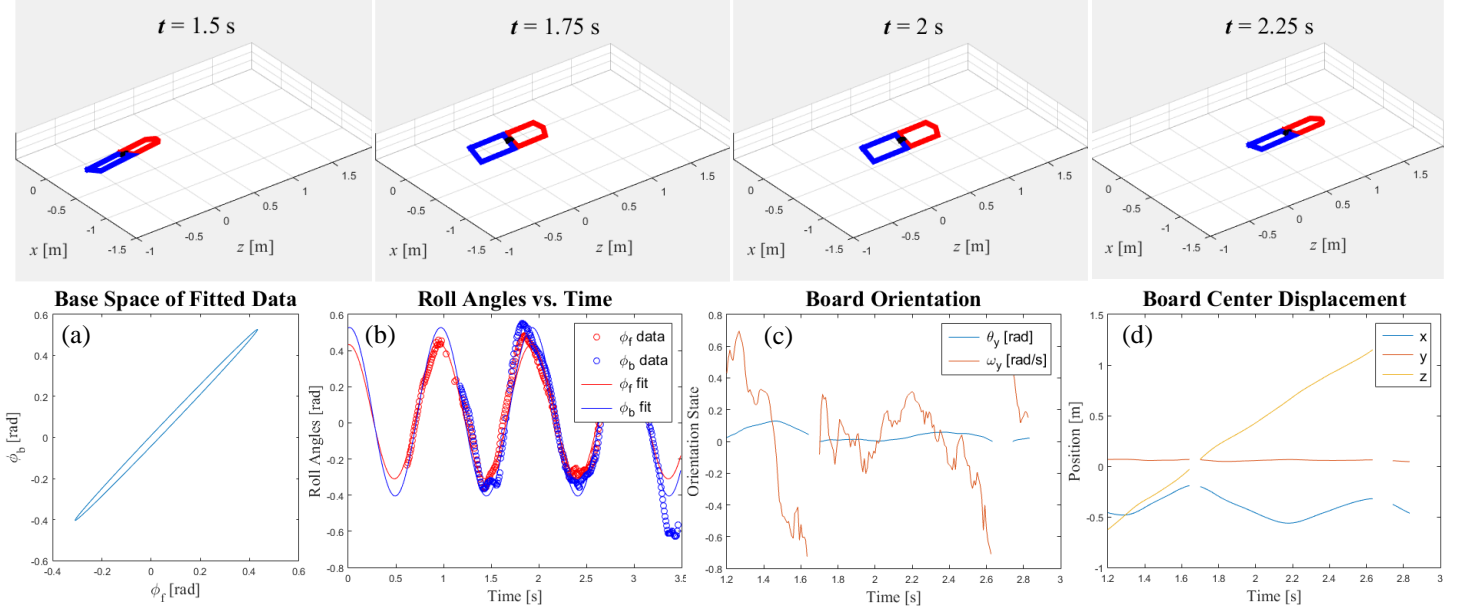


FIGURE 7. ALTERNATIVE GAIT FOR SUSTAINED FORWARD MOTION OF THE WAVEBOARD, IN WHICH FRONT AND REAR PLATFORMS OSCILLATE ENTIRELY IN PHASE. TOP ROW: ANIMATION SEQUENCES. BOTTOM ROW: PLOTS ILLUSTRATING (A) BASE SPACE OF FITTED DATA, AND TIME VARIATIONS OF (B) ROLL ANGLES, (C) BOARD ORIENTATION STATES, AND (D) BOARD CENTER DISPLACEMENT.

1.85 rad was calculated in rear platform motion relative to front platform motion by Eq. (28). Although this type of motion encloses a finite area in the base space, inspection of the ξ^z height map of Fig. 6(e) reveals that this type of motion is associated with negligible kinematic contribution ($I^{GEO} \approx 0$). We conclude that this traditional type of gait for sustained forward motion on the waveboard is purely dynamic. This experimental evidence supports the original hypothesis made by Shammass et al. [1] that this type of gait is purely dynamic.

An alternative gait for forward motion, in which front and rear platform oscillations are entirely in phase, is presented in Fig. 7. As expected, we obtain an ellipse with an upward sloping major axis and a high aspect ratio in the base space, which indicates negligible phase lag between front and rear platform motions. The geometric phase space represented by the small net volume enclosed underneath the ξ^z height function does not

contribute significantly to this gait, implying a purely dynamic gait. Once again, forward velocity remains fairly constant. Actual phase lag Δ_0 of fitted data, as defined in Eq. (28), was approximately 0.0562 rad for this gait.

A comparison between experimentally obtained and reconstructed displacements in the forward direction in the global frame is presented in Fig. 8. Displacements were computed through sequential application of Eq. (19), (8), and (18) for each gait. Reconstructed global displacements closely match the experimental data for short time intervals, supporting the validity of our model. Differences could be due to uncertainty in model parameters (especially mass and moment of inertia) and model assumptions (especially regarding friction). Accumulation of error with time is attributed to amplification of velocity error upon integration. Relatively higher error levels associated with reconstructing the alternative gait are associated

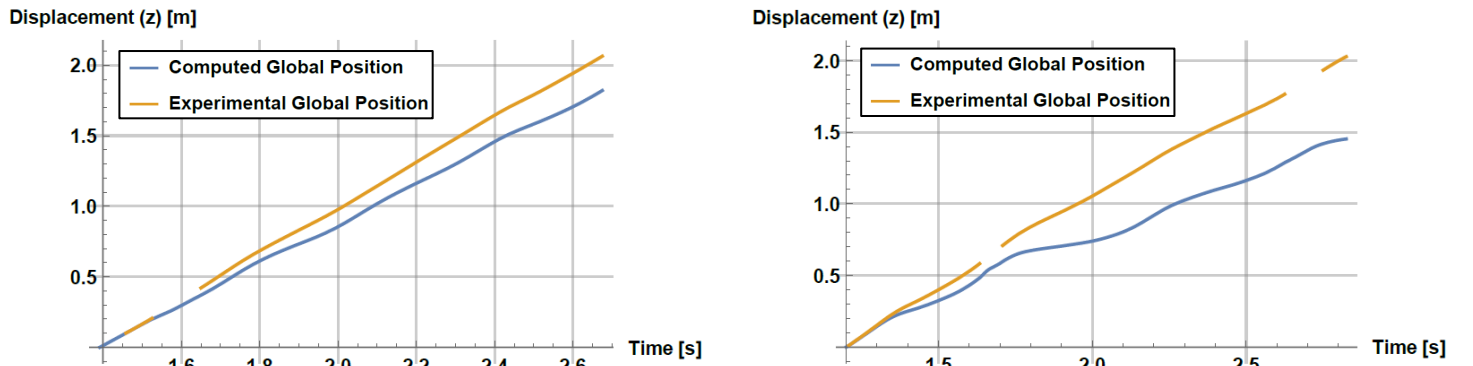


FIGURE 8. COMPARISON BETWEEN COMPUTED AND EXPERIMENTAL DATA FOR GLOBAL DISPLACEMENT IN FORWARD DIRECTION FOR TRADITIONAL GAIT (LEFT) AND ALTERNATIVE GAIT (RIGHT).

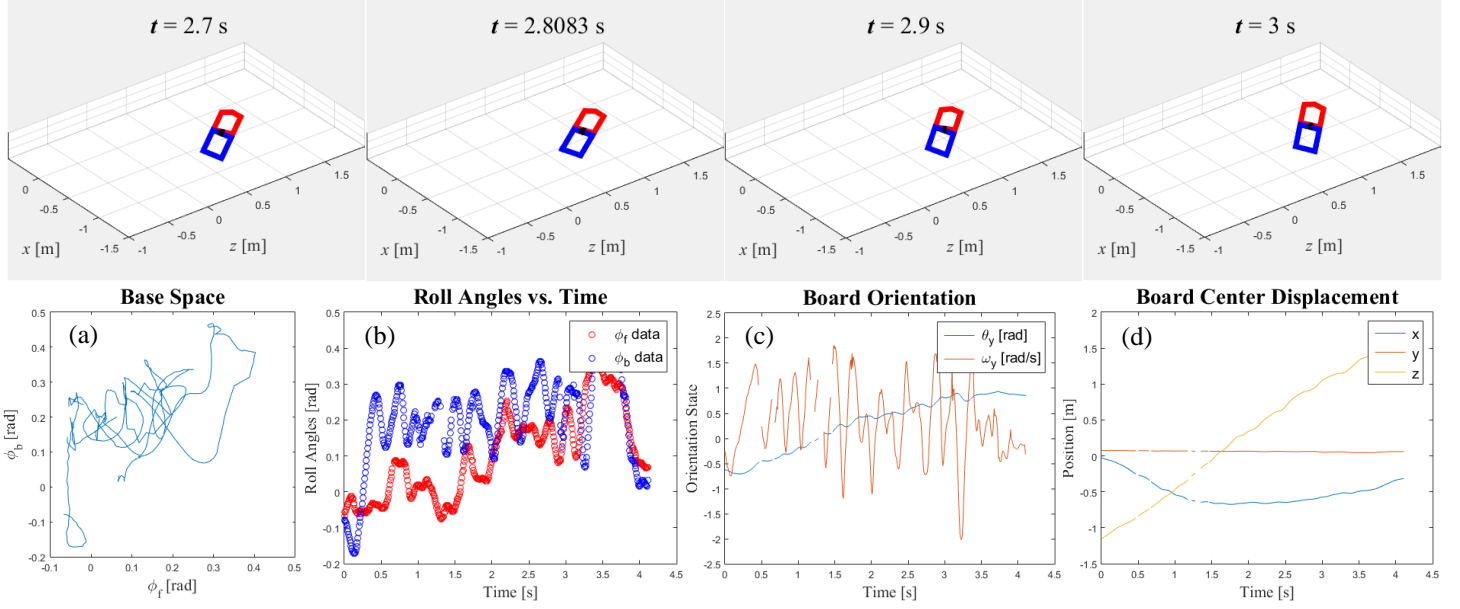


FIGURE 9. GAIT FOR COUNTERCLOCKWISE TURNING MOTION OF THE WAVEBOARD AT LOW SPEED. TOP ROW: ANIMATION SEQUENCES. BOTTOM ROW: PLOTS ILLUSTRATING (A) BASE SPACE OF ORIGINAL DATA, AND TIME VARIATIONS OF (B) ROLL ANGLES, (C) BOARD ORIENTATION STATES, AND (D) BOARD CENTER DISPLACEMENT.

with larger roll angles violating the aforementioned small angle assumptions to a greater extent, which is evident upon comparison of Fig. 6(b) and 7(b).

A gait for sustained counterclockwise turning motion is presented in Fig. 9. Since the time variations of roll angles do not follow the form of Eq. (27), the original data, rather than fitted data, was used to plot the base space in Fig. 9(a). Although the direction of motion in the base space is not specified, it can be assumed to be counterclockwise, since rear platform motion trails front platform motion by virtue of caster wheel incline associated with board directionality. Inspection of the height maps of Fig. 2 indicates that a counterclockwise motion in the upper right quadrant of the base space results in a significant positive kinematic contribution towards forward and angular displacement, but no significant kinematic contribution in the lateral body direction. We can conclude that this type of gait is not purely dynamic, and that turning motions depend directly on the rider's motions and potentially any momentum acquired by the system in order to both rotate and maintain forward velocity.

CONCLUSION

In review, height functions corresponding to forward, lateral, and rotary motion were obtained. Experimental gait reconstruction and curve fitting of base spaces to ellipses were accomplished for common types of gaits. By superimposing base space trajectories of experimental gaits onto height functions, we demonstrated that traditional forward motion on the waveboard is purely dynamic, and sustained turning motion contains a kinematic contribution.

Forward displacement in the global frame was computed for two types of gaits. Similarities between reconstructed and experimental displacements support our model of the

reconstruction equation. Differences could be used to tune model parameters in a future investigation.

A future study would involve computing the momentum using the momentum evolution equation presented in Eq. (23), as well as body velocities and body velocity integrals using the obtained generalized momentum. Through this framework, comparisons of output parameters between model and experiment corresponding to a given gait could be quantitatively analyzed. This would allow further experimental evaluation of the system model and its underlying assumptions, ultimately informing design and control of highly maneuverable robots.

ACKNOWLEDGMENTS

The authors thank Jin Dai for his assistance operating the OptiTrack Motive optical tracking system and Elie Shammas for his insight towards modeling mixed mechanical systems.

REFERENCES

- [1] Shammas, E.A., Choset, H. and Rizzi, A.A., 2007. Towards a unified approach to motion planning for dynamic underactuated mechanical systems with non-holonomic constraints. *The International Journal of Robotics Research*, 26(10), pp.1075-1124.
- [2] Ostrowski, J., Lewis, A., Murray, R. and Burdick, J., 1994, May. Nonholonomic mechanics and locomotion: the snakeboard example. In *Robotics and Automation, 1994. Proceedings., 1994 IEEE International Conference on* (pp. 2391-2397). IEEE.
- [3] Shammas, E.A., 2006. *Generalized motion planning for underactuated mechanical systems* (Doctoral dissertation, Carnegie Mellon University).

- [4] Shammass, E. and De Oliveira, M., 2012. Motion planning for the Snakeboard. *The International Journal of Robotics Research*, 31(7), pp. 872-885.
- [5] Dear, T., Hatton, R.L., Travers, M. and Choset, H., 2013, October. Snakeboard motion planning with local trajectory information. In *ASME 2013 Dynamic Systems and Control Conference* (pp. V002T33A002-V002T33A002). American Society of Mechanical Engineers.
- [6] Dear, T., Kelly, S.D., Travers, M. and Choset, H., 2015, May. Snakeboard motion planning with viscous friction and skidding. In *Robotics and Automation (ICRA), 2015 IEEE International Conference on* (pp. 670-675). IEEE.
- [7] Asnafi, A.R. and Mahzoon, M., 2007. Some flower-like gaits in the snakeboard's locomotion. *Nonlinear Dynamics*, 48(1-2), pp. 77-89.
- [8] Kinugasa, K., Ishikawa, M., Sugimoto, Y. and Osuka, K., 2013, September. Modeling and Control of Casterboard Robot. In *NOLCOS* (pp. 785-790).
- [9] Marsden, J.E. and Ratiu, T., 2013. *Introduction to mechanics and symmetry: a basic exposition of classical mechanical systems* (Vol. 17). Springer Science & Business Media.
- [10] Bloch, A., Baillieul, J., Crouch, P., Marsden, J.E., Krishnaprasad, P.S., Murray, R.M. and Zenkov, D., 2003. *Nonholonomic mechanics and control* (Vol. 24). New York: Springer.
- [11] Ostrowski, J.P., 1996. *The mechanics and control of undulatory robotic locomotion* (Doctoral dissertation, California Institute of Technology).
- [12] Hatton, R.L. and Choset, H., 2011. Geometric motion planning: The local connection, Stokes' theorem, and the importance of coordinate choice. *The International Journal of Robotics Research*, 30(8), pp. 988-1014.